

Promoted Glycerol Oxidation Reaction in an Interface-Confined Hierarchically Structured Catalyst

Zhongxin Chen, Cuibo Liu, Xiaoxu Zhao, Huan Yan, Jing Li, Pin Lyu, Yonghua Du, Shibo Xi, Kai Chi, Xiao Chi, Haisen Xu, Xing Li, Wei Fu, Kai Leng, Stephen J. Pennycook, Shuai Wang,* and Kian Ping Loh*

Confined catalysis in a 2D system is of particular interest owing to the facet control of the catalysts and the anisotropic kinetics of reactants, which suppress side reactions and improve selectivity. Here, a 2D-confined system consisting of intercalated Pt nanosheets within few-layered graphene is demonstrated. The strong metal–substrate interaction between the Pt nanosheets and the graphene leads to the quasi-2D growth of Pt with a unique (100)/(111)/(100) faceted structure, thus providing excellent catalytic activity and selectivity toward one-carbon (C1) products for the glycerol oxidation reaction. A hierarchically porous graphene architecture, grown on carbon cloth, is used to fabricate the confined catalyst bed in order to enhance the mass-diffusion limitation in interface-confined reactions. Owing to its unique 3D porous structure, this graphene-confined Pt catalyst exhibits an extraordinary mass activity of 2910 mA mg_{Pt}⁻¹ together with a formate selectivity of 79% at 60 °C. This paves the way toward rational designs of heterogeneous catalysts for energy-related applications.

Since its first demonstration in zeolites, interface-confined catalysis has emerged as a powerful method to control chemical reaction pathways in petroleum refining and petrochemical industries.^[1–3] For instance, zeolites with well-defined porous structures are able to discriminate reactants and products by their shape/size-dependent diffusivity in the pore channels. The size-exclusion of reactants, adsorption energy difference or steric hindrance of various products, restricted transition-state selectivity, and molecular traffic controls allow the alteration of selectivity

in interface-confined catalysis.^[3,4] These have been actively explored over the last decade in different material systems ranging from zeolites to metal-organic frameworks^[5] and carbon nanotubes.^[6]

In comparison with 0D- and 1D-confined systems, the vertically-confined growth of catalysts within a 2D space leads to preferred orientation and lattice strains.^[7] For instance, graphene plays a critical role in stabilizing intercalated 2D gallium nitride.^[8] Such encapsulation not only modulates the electron density of the active center to achieve extremely high activity, but also creates a unique quasi-2D confined space for robust catalysis with unexpected selectivity.^[9,10] Recently, Deng et al. reported the oxidation of benzene to phenol at room temperature using encapsulation of a single FeN₄ site catalyst in a graphene matrix.^[11]

The confinement of Pt^[12] and Co(OH)₂ nanoparticles^[13] within the layered spacing of MoS₂ have also been shown to lead to enhanced activity and stability for water splitting.

Although the restricted space in 2D-confined systems potentially allows shape/size selectivity of the reactants and products, it is disadvantaged by sluggish reaction kinetics due to diffusion limitations.^[6,7,12] One strategy to allow vertical diffusion, other than in-plane diffusion through the interlayers, is to create porosity in the graphene sheets that are confining the catalysts. The construction of 3D nanostructures with macropores is also favorable for the exposure of active sites to relevant

Z. Chen, Dr. C. Liu, X. Zhao, Dr. H. Yan, Dr. J. Li, P. Lyu, Dr. X. Chi, Dr. H. Xu, X. Li, Dr. W. Fu, K. Leng, Prof. K. P. Loh
Department of Chemistry and Centre for Advanced 2D Materials (CA2DM)
National University of Singapore
3 Science Drive 3, Singapore 117543, Singapore
E-mail: chmlhkp@nus.edu.sg

Z. Chen, X. Zhao, X. Li, Prof. S. J. Pennycook, Prof. K. P. Loh
NUS Graduate School for Integrative Sciences and Engineering
National University of Singapore
Centre for Life Sciences
#05-01, 28 Medical Drive, Singapore 117456, Singapore

 The ORCID identification number(s) for the author(s) of this article can be found under <https://doi.org/10.1002/adma.201804763>.

Dr. Y. Du, Dr. S. Xi
Department of Physics and Singapore Synchrotron Light Source
National University of Singapore
Singapore 119077, Singapore

K. Chi, Prof. S. Wang
Key Laboratory of Material Chemistry for Energy Conversion and Storage
Ministry of Education
School of Chemistry and Chemical Engineering
Huazhong University of Science and Technology
Wuhan 430074, P. R. China
E-mail: chmsamuel@mail.hust.edu.cn

Prof. S. J. Pennycook
Department of Materials Science and Engineering
National University of Singapore
Singapore 117575, Singapore

DOI: 10.1002/adma.201804763

species to achieve a high apparent activity.^[7] However, catalyst engineering of such hybrid catalytic systems to allow both out-of-plane as well as in-plane diffusion of reactants and products remains largely unexplored.^[14]

Herein, we report a facile and productive synthesis method to sandwich Pt nanosheets in few-layered graphene. Essentially, Pt ions were intercalated into few-layered graphene and then reduced to their zero-valent state for the growth of Pt nanosheets in graphene (Pt-in-GN). The synergetic host-guest interaction in Pt-in-GN provides extraordinary catalytic activity and selectivity toward the glycerol oxidation reaction (GOR). In such a confined environment, most glycerol molecules experience a fast and complete decomposition to one-carbon (C1) products. We further exploited a 3D hierarchically porous structure to address the mass diffusion limitation of the interface-confined reaction, where the confined Pt nanosheets in a vertically grown graphene nanomesh exhibit extraordinary catalytic performance (≈ 2.5 times in mass activity) compared with the benchmark 10% Pt/C even at reduced Pt loading.

Layered materials are promising in hosting catalytically active materials, such as zero-valent transition metals, in their interlayer spacing to enhance the activity and stability.^[12,15,16] Such encapsulation usually involves an isothermal vapor transport method to intercalate metal chlorides above their sublimation points under a pressure of chlorine gas, which is extremely dangerous and time-consuming.^[17] It is also difficult to control the morphology of encapsulated transition metals via subsequent alkali metal reduction, yielding amorphous nanoparticles with a diameter of 3–10 nm.^[16] For better shape control, we developed a new method for liquid-phase Pt ion encapsulation and control of the morphology of Pt domains by H₂ reduction. As shown in **Figure 1a**, the PtCl₄ intercalated graphene (PtCl₄-in-GN) was prepared by the reaction of H₂PtCl₆ with few-layered graphene in thionyl chloride. Subsequently, the PtCl₄ precursor was reduced under H₂ gas at 600 °C to form nicely packed, quasi-2D Pt nanosheets. Such sandwiched Pt-in-GN is extraordinarily active toward the GOR in comparison with the benchmark 10% Pt/C, together with a unique selectivity to C1 products from the confined, quasi-2D nature.

The quasi-2D Pt nanosheets within few-layered graphene were characterized by scanning electron microscopy (SEM) and scanning transmission electron microscopy in the annular dark field mode (STEM-ADF), as shown in **Figure 1**, and in **Figures S1–S3** in the Supporting Information. The SEM images reveal a loosely stacked morphology after Pt encapsulation. Due to the confinement effect and strong charge-transfer between PtCl₄ and neighboring graphene nanosheets, the grown Pt nanocrystals adopt a quasi-2D morphology with a thickness of 4–7 nm after H₂ reduction, as seen from the atomic force microscopy (AFM) images in **Figure S5** in the Supporting Information. The co-existence of Pt nanosheets and graphene superlattices in **Figure S4** in the Supporting Information further confirms successful encapsulation within the graphene layer spacing,^[18] while no Pt nanoparticles could be observed on the surface or edge of graphene in the TEM images. In comparison, solution deposition of Pt nanoparticles on graphene produces an inhomogeneous distribution, with many large aggregates of up to tens of nanometers in size. It is worth pointing out that the growth of Pt nanosheets is extremely challenging, where a secondary metal, such as Pd is necessary to reduce the high surface energy.^[19]

The atomic-resolution STEM-ADF image and corresponding fast Fourier transform (FFT) pattern in **Figure 2a,b** indicate that the Pt nanodomains reveal two sets of distinct crystal facets, and the obtained FFT spots identify (100) and (111) facets as highlighted by the blue and red circles, respectively. The presence of two well-defined facets in the Pt nanosheets is further corroborated by the inverse FFT, as shown in **Figure 2c,d**, which reveals a distinct contrast pattern. The lattice parameter of bulk crystalline Pt is ≈ 0.28 nm. However, in the sandwiched Pt nanosheets, the lattice parameter along the [010] direction in the (100) plane reveals a significant tensile strain with the Pt–Pt bond elongated to 0.32 nm. The simulated images along (100) and (111) zone axes depicted in the right panels perfectly resemble the experimental results. The enlarged atomic-resolution STEM-ADF image (**Figure 2f**) clearly reveals the combined atomic packing information originated from both (100) and (111)

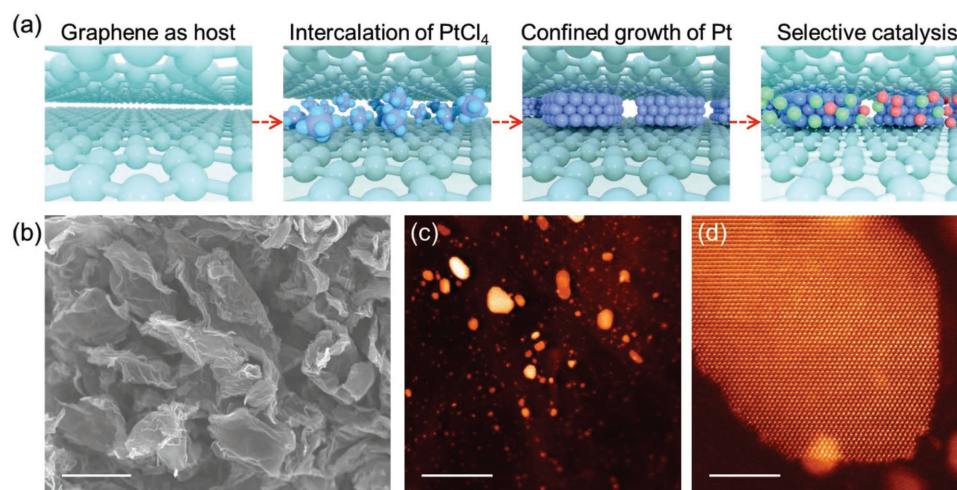


Figure 1. a) Schematic of the Pt sandwiched structure in few-layered graphene and subsequent selective catalytic reaction in a confined, quasi-2D environment. b) Representative SEM and c,d) STEM images at different magnifications. Scale bars: (b) 5 μm ; (c) 50 nm; (d) 5 nm.

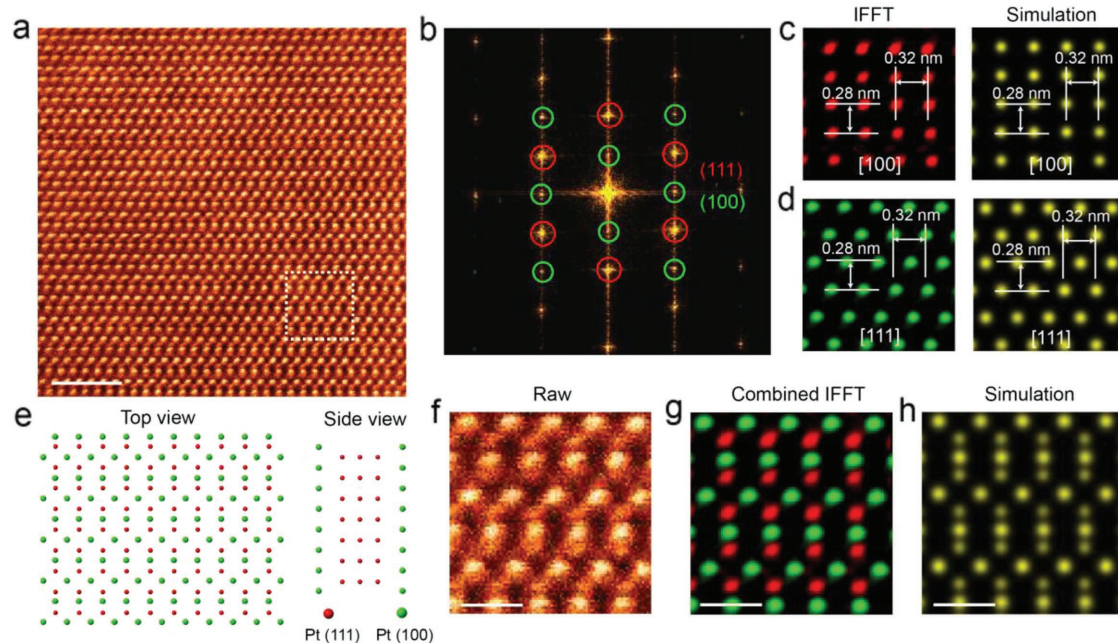


Figure 2. Electron microscopy study of the sandwiched Pt nanosheets. a) An atomic-resolution STEM-ADF image of a sandwiched Pt nanosheet in few-layered graphene, and b) the corresponding FFT pattern. Characteristic diffraction spots originating from the (100) and (111) zone axis, respectively, are highlighted by green and red circles. c,d) Inverse FFT of the white box region in (a) by masking the characteristic (100) (c) and (111) (d) FFT spots. Corresponding simulated images are depicted in the right panels. e) Schematic illustration of the sandwiched Pt nanosheets revealing two types of crystal facets where (111) and (100) are marked by red and green, respectively. f) Enlarged white box region in (a). g) Combined IFFT pattern of (100) facet (c) and (111) facet (d). h) Corresponding simulated image derived from the atomic model shown in (e). Scale bars: (a) 2 nm; (f–h) 0.5 nm.

images in Figure 2g. Therefore, the as-grown Pt nanosheets are predominantly composed of (100) and (111)-textured domains, as schematically illustrated in Figure 2e.

This unique packing of Pt-in-GN is remarkably different from the mixed facets in conventional Pt/C catalysts, where the latter is in a close packed face-centered cubic structure with only one facet in a given direction.^[9] Previous results on Pt nanosheets with secondary metals also exhibit only one facet for the basal plane of the nanosheets.^[19] Our observation of two well-defined facets along the vertical direction suggests that interfacial strain plays a role in the growth of the crystal planes. Pt₃₀₉ (100) on graphene has much lower strain (<2%) in comparison with ≈4% strain for Pt₃₀₉ (111) on graphene.^[20] To minimize interlayer strain, the first layer grown on graphene is Pt (100) and this transforms into the (111) facets as thickness increases. Due to the sandwiching effect by graphene on either side, a mixed phase Pt (100) | Pt (111) | Pt (100) structure forms. The (100) facet has a lower coordination number than (111) (4 vs 6), thus the under-coordinated Pt atoms may serve as active sites for electrocatalysis.

The changes produced in the graphene lattice by intercalation and H₂ reduction were studied by Raman spectroscopy. As shown in Figure 3a,b, pristine graphene shows two characteristic bands at 1587 (G band) and 1358 cm⁻¹ (D band), corresponding to contributions from sp² hybridized aromatic carbon and sp³ type carbon from defects.^[21] The presence of the 2D band at 2719 cm⁻¹ together with a small I_D/I_G ratio of 0.12 clearly indicates a well-preserved aromatic structure for the graphene. The I_{2D}/I_G ratio is ≈0.32, corresponding to that of 3–4 layered graphene.^[21] After PtCl₄ intercalation, an additional

shoulder at 1611 cm⁻¹ is observed for the G band of the graphene layer adjacent to PtCl₄ intercalants.^[22] The D band is also much stronger compared to that found in pristine graphene, with an increased I_D/I_G ratio of ≈0.68. Meanwhile, the 2D peak for PtCl₄-in-GN also downshifts to 2681 cm⁻¹ due to the charge transfer between PtCl₄ and graphene.^[17] The reduction of PtCl₄ to its zero-valent state recovers the disturbance in the aromatic structure, reflected by a reduced D band, the disappearance of the intercalation peak, and a backshift of the 2D band to its original position.

X-ray diffraction (XRD) is a powerful technique for characterizing the structural evolution for intercalated materials. As shown in Figure 3a, reflections from the parent few-layered graphene were essentially indiscernible at low angles, with the observed, weak, and very broad reflections at ≈13.5° assigned to a stage III intercalated compound with PtCl₄ (0.66 nm).^[17] This is also validated by the 1D and 2D spectra of grazing incidence X-ray diffraction (GIXRD) in Figure S6 in the Supporting Information. Unfortunately, the intercalation peak of G | Pt | G sandwich at ≈1° is beyond the detection limit of XRD and GIXRD, where Pt-in-GN only shows a noisy background at low angles.^[12] We further utilized XRD to characterize the crystalline structure of graphene and Pt nanodomains. Unlike the amorphous morphology of common intercalated compounds, we observe very strong XRD peaks assignable to the (111), (200), and (110) planes of Pt, indicating a neat packing structure for the Pt nanosheets, as shown in Figure 3d.^[12] The (002) diffraction peak at 26.3°, which measures the interlayer lattice distance, is reduced in intensity and broadened after Pt intercalation,

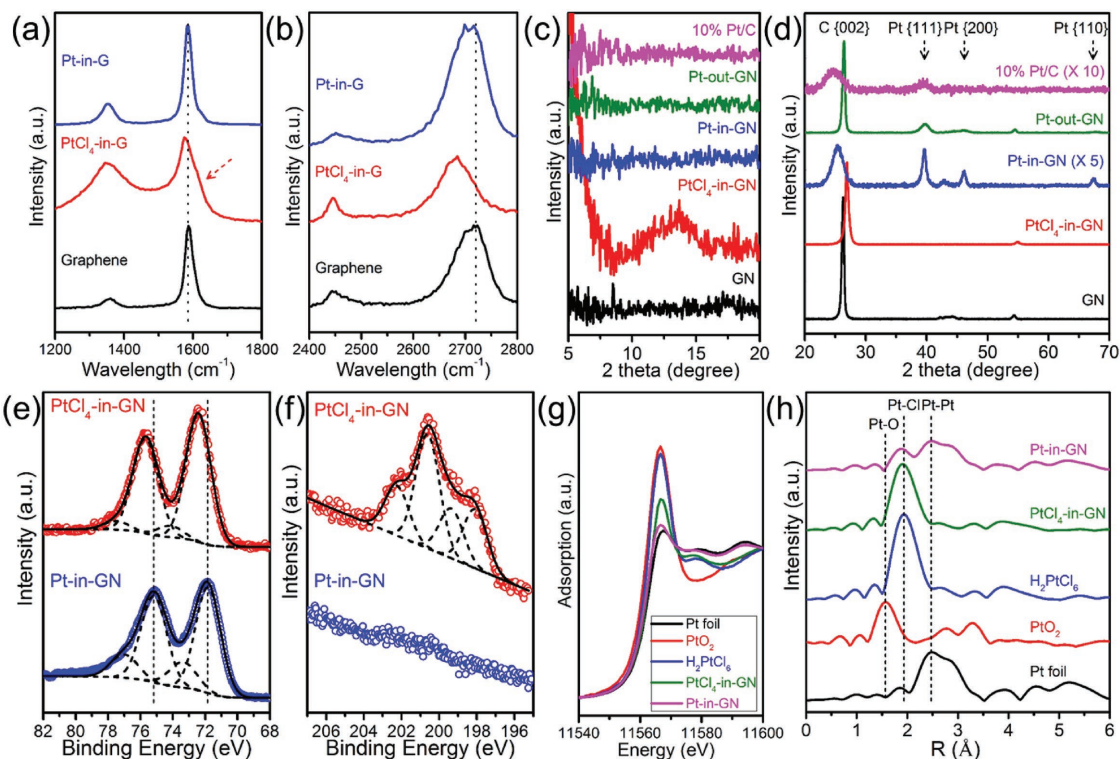


Figure 3. Evidence of the sandwiched Pt nanosheets. a,b) Raman spectra of graphene, PtCl₄-in-GN and Pt-in-GN; c,d) XRD patterns of graphene, PtCl₄-in-GN, Pt-in-GN, Pt-out-GN, and 10% Pt/C; e) Pt_{4f} and f) Cl_{2p} XPS spectra; g) Pt L-edge XANES and h) EXAFS spectra of Pt foil, PtO₂, H₂PtCl₆, PtCl₄-in-GN, and Pt-in-GN.

indicating the successful intercalation of Pt domains within the graphene interlayer spacing.

Meanwhile, the chemical composition before and after H₂ reduction was verified by XPS. The Pt_{4f} core-level spectrum for PtCl₄-in-GN is shown in Figure 3e; it consists of the spin-orbit doublets Pt 4f_{7/2} and 4f_{5/2}, which show different peak positions for the intercalated PtCl₄ and H₂PtCl₆ species at 72.4 and 75.7 eV and at 74.1 and 77.5 eV, respectively. After H₂ reduction, the peaks are shifted to 71.8 and 75.1 eV for the Pt(0) species alongside a peak shift to 73.4 and 77 eV for the PtO species.^[23] The reduction of the Pt precursor is further evidenced by the disappearance of the Cl_{2p} signal in Pt-in-GN in Figure 3f. More importantly, the Pt(0) peaks shift to a higher binding energy in comparison with those of 10% Pt/C, indicating electron delocalization in the quasi-2D system and electron transfer from Pt to graphene.^[24] Such a strong metal-substrate interaction is beneficial to catalytic performance. For instance, Jiang et al. observed a significantly enhanced oxygen reduction reaction (ORR) stability for a Pt/MWCNT-TiO₂ catalyst compared to the benchmark Pt/C due to the anchoring effect and strong metal-support interaction.^[25] We can also observe a strong C–C peak at 284.8 eV and a small C–O tailing at 286.8 eV in the C_{1s} spectra, suggesting that the graphene aromatic structure is well preserved following PtCl₄ intercalation and H₂ reduction. This is confirmed by the near-edge X-ray absorption spectroscopy (XAS) spectra shown in Figure S7 in the Supporting Information, where the three peaks are assigned to the sp² unoccupied π* band, C=O species, and sp² unoccupied θ* band.^[26] The preservation

of the π-π conjugate structure is important for the electrical conductivity of the catalyst and the electron transfer process during electrocatalysis.

The chemical state and local bonding environment in Pt-in-GN were investigated by X-ray absorption near-edge structure (XANES) and extended X-ray absorption fine structure (EXAFS). The Pt L₃-edge XANES spectrum of PtCl₄-in-GN is analogous to that of H₂PtCl₆ in terms of edge position in Figure 3g.^[27] After H₂ reduction, Pt is converted to its zero-valent state with an identical XANES profile to Pt foils. In addition, the Fourier transforms of EXAFS spectra for H₂PtCl₆ and PtCl₄-in-GN exhibit an apparent Pt–Cl peak at 1.96 Å. The peak intensity is lower in the case of PtCl₄-in-GN owing to its lower coordination number of Pt atoms.^[28] A significant metallic Pt–Pt peak appears and the Pt–Cl peak reduces after H₂ reduction, which is characteristic of the conversion to the zero-valent state. The sandwiched Pt nanosheets are well-protected and no Pt oxides could be seen in the XANES and EXAFS spectra. The surface area and porosity of catalysts were determined by Brunauer–Emmett–Teller (BET) measurements. As shown in Figure S8 in the Supporting Information, Pt-in-GN shows a type-IV N₂ isotherm with a distinct hysteresis loop at P/P₀ = 0.4–1.0 together with a relatively high surface area than 10% Pt/C (348.7 vs 215.6 m² g⁻¹) owing to its few-layered structure. The pore size distribution from BET is dominated at 4.0 nm, which is consistent with the thickness of Pt nanosheets in the interlayer spacing.

The Pt-in-GN powder catalyst suffers from poor mass diffusion due to the confined space where the catalysts are sandwiched. To improve the mass diffusion, a vertically erected,

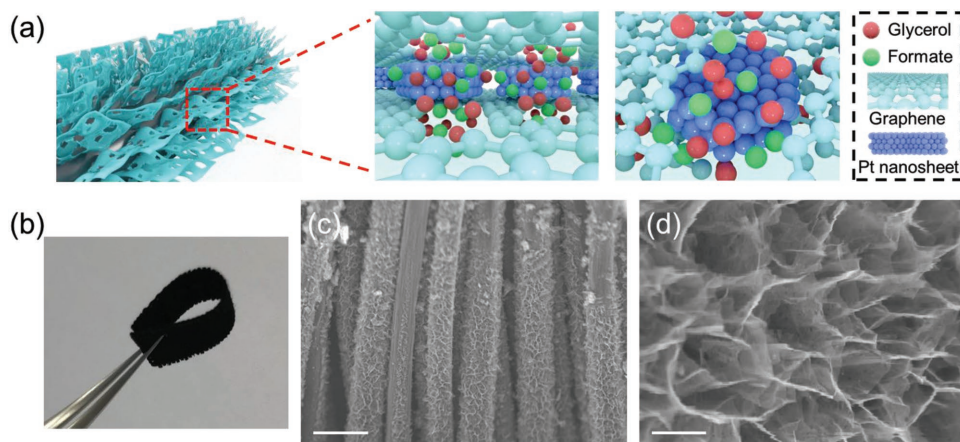


Figure 4. The growth of Pt nanosheets within vertically grown graphene array. a) Schematic of the interface-confined reaction in the 3D hierarchically porous catalyst; b) digital photo of as-prepared Pt-in-VGCC; c, d) SEM images of Pt-in-VGCC at different magnifications. Scale bars: (c) 20 μm ; (d) 1 μm .

nanoporous graphene wall structure was used as the electrode.^[6,10] Due to its exposed edges as well as porosity, such a structure affords pathways for the diffusion of reactants and products through the plane as well as the edges, as shown in Figure 4a.

The N-doped vertically grown graphene nanomesh on carbon cloth (VGCC) was prepared by $\text{Ni}(\text{OH})_2$ templating and subsequent carbonization of polydopamine. The vertical structure of the graphene array on carbon fibers is verified by SEM images in Figure 4, and in Figure S17 in the Supporting Information. Numerous macropores with size of several microns could be found between the interconnected graphene flakes. The high-resolution SEM image in Figure 4c further confirms the existence of nanopores on as-grown graphene from the leaching process of $\text{Ni}(\text{OH})_2$ templates and gas release in the pyrolysis

of polydopamine. Owing to this hierarchical porous structure, Pt encapsulation in VGCC can be carried out using the same procedure to achieve a mass loading of $0.05 \text{ mg}_{\text{Pt}} \text{ cm}^{-2}$ for Pt-sandwiched graphene nanomesh on carbon cloth (Pt-in-VGCC, Figure S18, Supporting Information). Such an approach is highly scalable and offers great advantages to fabricate large area Pt-confined carbon cloth electrodes with the desired size and shape for application in glycerol fuel cells, as shown in Figure 4b.

We selected GOR to evaluate the catalytic performance of interface-confined catalysts. GOR is a complex reaction in alkaline solution, giving multiple products such as glyceric acid, tartronic acid, and other C2 or C1 products via C–C bond breaking, as shown in Figure 5a.^[29] The operation of a direct glycerol fuel cell offers the economic advantage of coproducing

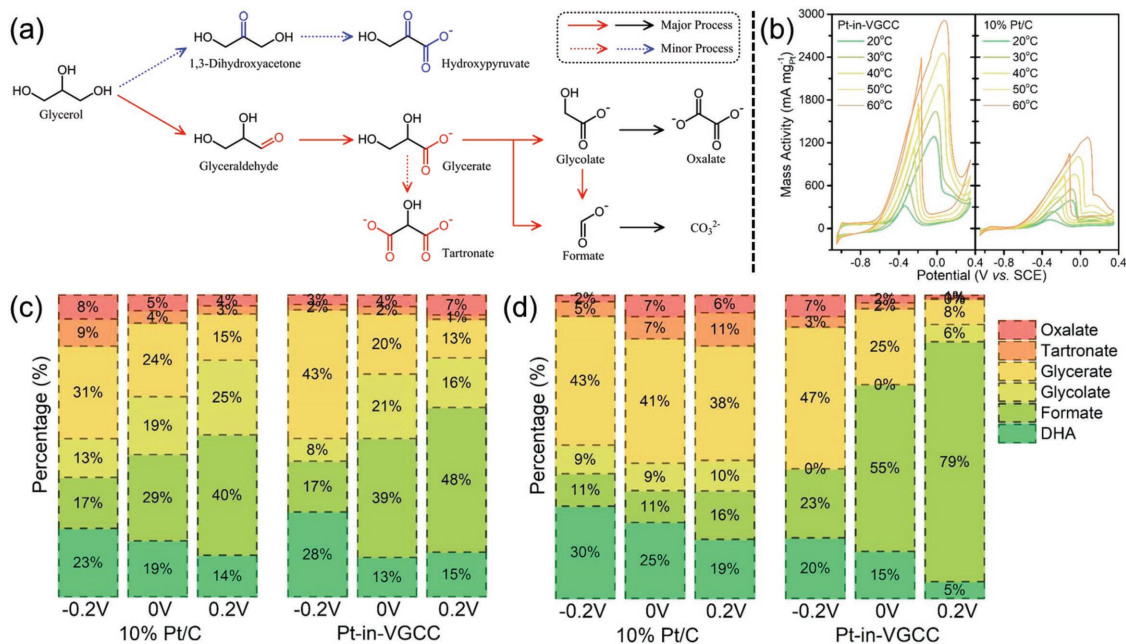


Figure 5. GOR in a confined space. a) GOR pathway for Pt-based catalysts. b) Comparison in the mass activity of Pt-in-VGCC and 10% Pt/C. c) Products of glycerol oxidation at 20 °C and d) 60 °C from HPLC analysis. Pt loading: $\approx 0.05 \text{ mg}_{\text{Pt}} \text{ cm}^{-2}$ for Pt-in-VGCC and $0.1 \text{ mg}_{\text{Pt}} \text{ cm}^{-2}$ for 10% Pt/C.

electricity and chemical products, however, the maximum charge which can be extracted is limited by incomplete oxidation reactions.^[30] In this regard, interface-confined reactions may increase the residence time of the reactants to facilitate a more complete oxidation process than an open reaction system where diffusion of reactants from the electrode occurs before complete oxidation.

We employed the standard electrode fabrication techniques in fuel cells to examine the GOR activity from 20 to 60 °C, as shown in Figure 5, and in Figures S9 and S10 in the Supporting Information. Both 10% Pt/C and Pt-in-GN (5.6 wt% Pt from inductively coupled plasma (ICP), Table S1) were loaded on a poly(tetrafluoroethylene) (PTFE)-treated carbon paper at a loading of 1 mg cm⁻², where Pt-in-VGCC was directly used as working electrode without any further modification.

The GOR activity of Pt-in-VGCC was investigated by the CV profiles, as shown in Figure 5b. We found that Pt-in-VGCC exhibits much higher current densities than 10% Pt/C even at a 50% reduced Pt loading. This leads to an extraordinary mass activity of 2910 mA mg_{Pt}⁻¹ at 60 °C, which is ≈2 times higher than that of Pt-in-GN (1420 mA mg_{Pt}⁻¹), and is among the most efficient Pt-based catalysts for GOR, as listed in Table S2 in the Supporting Information.^[30–34] The superior performance of Pt-in-VGCC can be attributed to its unique 3D porous structure, which facilitates the mass diffusion of reactants into the inner surface of Pt nanosheets. The strong metal–substrate interaction between Pt nanosheets and graphene^[25] and the confinement effect further improve the selectivity of the catalysis.^[12] Even after a continuous operation at 60 °C for 2 h, the mass activity of Pt-in-VGCC retains a relatively high value (≈300 mA mg_{Pt}⁻¹), as shown in Figure 6, suggesting that it is stable against poisoning by reaction intermediates. Furthermore, >85% of the GOR activity can be recovered by a simple electrode cleaning process in 1 M KOH electrolyte to remove the surface-absorbed molecules for carbon paper electrodes, as shown in Figure S15 in the Supporting Information. The morphology and catalytic performance also remain stable after five continuous GOR measurements (5 × 2 h, cleaned in KOH electrolyte) using the Pt-in-VGCC electrode, as shown in Figure S19 in the Supporting Information.

The GOR products using Pt-in-VGCC were then monitored by high-performance liquid chromatography (HPLC) after holding at a particular potential for 2 h. As depicted in Figure 5c,d, glycerate, glycolate, and formate are the main C3,

C2, and C1 products in GOR, suggesting the reaction undergoes primary alcohol oxidation and subsequent C–C bond cleavage. A certain amount of 1,3-dihydroxyacetone (DHA) is detected by HPLC. Trace amount of glyceraldehyde (GAD) and hydroxypyruvate, if present in the reaction products, are not detectable.^[35] The selectivity toward C1 product (formate) becomes higher at high oxidation potentials, which is reasonable as the oxidation of C2 (oxalate) and C3 products (tartarate etc.) only happens at relatively high potentials. Owing to the confined environment and unique 3D porous structure, the selectivity toward formate reaches ≈79% at 0.2 V at 60 °C, while the fraction of C2 and C3 products reduces to 8% and 13%. This suggests most glycerol molecules are quickly and completely converted to formates and carbonates.^[30] Meanwhile, the reaction products change only slightly for 10% Pt/C at various potentials, which indicates the adsorption/reaction of GOR-related intermediates are less influenced on exposed Pt nanoparticles by reaction temperature. The above results are supported by the detailed mechanistic investigation on the GOR intermediates using a 3 mm glassy carbon (GC) working electrode, as shown in Figures S11–S14 in the Supporting Information.^[35–37]

We have also conducted control experiments using lower H₂ reduction temperature and by using a conventional impregnation method, as shown in Figure S16 in the Supporting Information. The Pt-in-GN obtained at lower reduction temperature (200 °C) only exhibits a low GOR activity in the 3 mm GC electrode measurement owing to the lower crystallinity of Pt nanodomains and weaker interaction between Pt and graphene.^[25,32] Meanwhile, the traditional impregnation approach only produces low Pt loading (4.9 wt% from ICP) with some large aggregations (>20 nm); this can be seen from the TEM images in Figure S16 in the Supporting Information, which is due to the lack of anchoring points for metal precursor in physically exfoliated few-layered graphene, leading to a low measured GOR activity.

Our interface-confined growth offers significant advantages for the growth of clean Pt metal nanosheets and allows strong metal–substrate interaction between the graphene host and sandwiched metals. Owing to its high surface energy, zero-valent metal nanosheets are typically thermally unstable and quickly pulverize into small nanoparticles. Previous efforts on the 2D growth of metals primarily involve the ligand-assisted colloidal methods, where specific facets are capped by capping agents.^[38–40] For instance, Zheng and co-workers reported the strong adsorption of CO molecules on the basal (111) planes of Pd nanosheets, which prevents growth along the (111) direction and directs the formation of the sheet-like structures.^[38] However, such nanocrystals are usually capped by inactive surfactants and polymers, which decreases the electrocatalytic activity significantly compared to surface-clean nanocrystals.^[39] The growth of Pt nanosheets is also extremely challenging, where both ligands and secondary metals (e.g., Pb^[19] or Cu^[41,42]) have to be used to stabilize the Pt nanosheets. Previous approaches for metal intercalation typically first exfoliate the 2D materials in solution, followed by flocculation of the exfoliated sheets in the presence of metal salt precursors, and finally reducing the trapped metal ions between the sheets to their zero-valent states. Sandwiched catalysts produced by

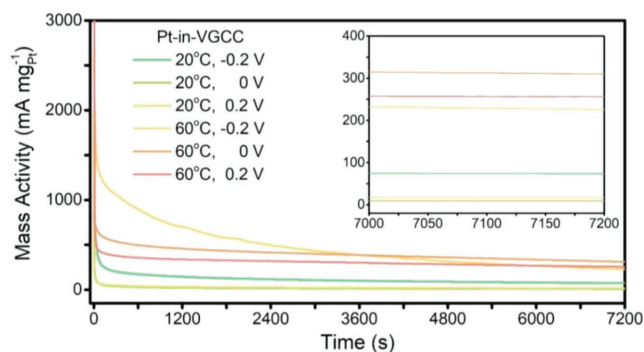


Figure 6. Stability of Pt-in-VGCC on glycerol oxidation.

such methods only have loosely packed morphology and their catalytic performance is very similar to exposed metal catalysts loaded on conventional supports.

The confined microenvironment around the active Pt nanosheets has a profound influence on the activity and selectivity of GOR. In addition, the morphology and catalytic properties of Pt nanosheets can be well-maintained even after high-temperature annealing at 600 °C owing to the unique G | Pt | G sandwiched structure. A recent theoretical study reveals the weakened adsorption of atoms and molecules on Pt (111), (110), and (100) surfaces under monolayer graphene cover due to the geometric constraint and confinement field effects.^[43] It is likely a weakened adsorption of glycerol occurs on interface-confined Pt nanosheets, thus promoting the GOR underneath the 2D overlayers. Meanwhile, the higher selectivity toward C1 products can be explained by increased local concentration and prolonged residence time of reactants in the confined space, leading to higher collision probability of reactants with the active sites and complete reaction. This is supported by an in situ Fourier transform infrared (FT-IR) spectroscopy investigation by Zalineeva et al.,^[34] where the confinement of reactants and intermediates in Pb_xBi pores is responsible for the high selectivity for GOR. The altered molecular motion by physical hindrance may also contribute to the GOR selectivity, however, their relationship is still unclear due to the complexity of the GOR reaction.

The confined growth of Pt nanosheets in few-layered graphene has been realized via the solution intercalation of Pt ion precursors following by H₂ reduction at high temperature. Owing to the strong confinement effect, the Pt nanosheets consist of mixed stacking of (100) and (111) facets and are different morphologically from Pt nanocatalysts grown by conventional colloidal methods in open conditions. Interface-confined Pt nanosheets also exhibit a much stronger oxidation and C–C bond cleaving ability for GOR, leading to a superior mass activity and selectivity toward C1 products than commercial 10% Pt/C catalysts. To enhance mass diffusion, we intercalate Pt nanosheets in a vertically-erected graphene nanowall electrode and achieve a very high glycerol oxidation rate of 2910 mA mg_{Pt}⁻¹ and a 79% selectivity toward formate at 60 °C. Therefore, our work presents a new strategy for enhancing mass diffusion in interface-confined reactions by using vertically-erected porous graphene scaffolds for the confinement of Pt nanosheets, where higher catalytic activity at reduced catalyst loading is obtained as compared to the open-catalyst system.

Experimental Section

Growth of Pt Nanosheets in Few-Layered Graphene: A total of 1.18 g of few-layered graphene (≈0.8 nm thickness, XF001W from Nanjing XFANO Materials Tech Co., Ltd) and 0.804 g of chloroplatinic acid hexahydrate (H₂PtCl₆·6H₂O) were added to 20 mL of SOCl₂. The mixture was then stirred for two days followed by sonication for 4 h prior to reflux at 83 °C for 4 h.^[17] After cooling down to room temperature, 40 mL of toluene was added to the mixture, with the product (PtCl₄-in-GN) filtered and washed with toluene, ethanol, water, and acetone before drying overnight at 80 °C. To grow Pt nanosheets, 100 mg of the precursor (PtCl₄-in-GN) was loaded into a quartz tube mounted inside a tube furnace under H₂ gas and then heated at 600 °C for 4 h to obtain Pt nanosheets in few-layered graphene. For comparison, Pt nanoparticles loaded onto graphene nanosheets (Pt-out-GN, 10 wt%) were prepared

by a solution method using ammonia borane as a reductant. The growth of Pt nanosheets in VGCC (provided by Prof. Shuai Wang) was carried out following the same procedure as Pt-in-GN.

Electrocatalysis: Glycerol oxidation was performed on an Autolab PGSTAT30 with a 3-electrode cell using a Pt plate and saturated calomel electrode (SCE) as the counter and reference electrodes. Catalyst ink was prepared by dispersing 5 mg of catalysts in 0.2 mL of water, 0.8 mL of ethanol, and 20 μL of 5% Nafion solution with sonication. Then, 200 μL of catalyst ink was dropped onto carbon paper (1 × 1 cm², Toray paper 120-PTFE treated) to achieve a catalyst loading of 1 mg cm⁻². The as-prepared working electrode was immersed in 10 mL of 0.1 M glycerol and 1 M KOH electrolyte with N₂ bubbling during the test. After holding at -0.2, 0, or 0.2 V versus SCE for 2 h, 0.75 mL of the solution was collected and neutralized with 0.75 mL of 0.5 M H₂SO₄ for HPLC analysis (Agilent 1200 with UV detector and Agilent Poroshell HILIC-Z column). The eluent was 7:3 acetonitrile/phosphate buffer solution (30 × 10⁻³ M K₂HPO₄ and 0.075% H₃PO₄, pH = 6.7). During the test, 10 μL of the sample was injected into the column with a flow rate of 0.8 mL min⁻¹ and a temperature of 30 °C. Calibration curves were obtained using standard solutions of products. The Pt-in-VGCC were directly used as working electrodes without any further modification. For the oxidation of various products, a 3 mm GC electrode at 0.3 mg cm⁻² catalyst loading was used as working electrode while other conditions were kept constant. To ensure the catalytic activity was not affected by the conversion and to guarantee a fast mass diffusion by concentration diffusion, glycerol was always in large excess during the GOR measurements, whose conversion was lower than 10% from the standard curves of products in HPLC measurements. The error in the distribution of GOR products should be smaller than 5%.

Material Characterization: The following equipments were used: STEM/EDS (JEOL ARM200F equipped with ASCOR probe corrector, Oxford X-Max 100TLE, at 200 kV), SEM/EDS (JEOL JSM-6701F), TEM (FEI Titan, 80 kV), Raman (WITec Alpha 300R), AFM (Dimension Fast Scan), XPS/XAS (SSLS, SINS beamline), and XRD/GIXRD (Bruker D8 and GADDS). XANES/EXAFS: 100 mg of sample was first ground into fine powder using a mortar and pestle before being pressed into a 10 mm pellet. To minimize moisture uptakes, ≈20 mg of H₂PtCl₆ was mixed with ≈100 mg of BN powder. Measurements were carried out at the Singapore synchrotron light source (SSLS), X-ray absorption fine structure for catalysis (XAFCA) beamline.^[44] Data analysis and simulation were carried out on Athena, Artemis, and Hephæstus (version 0.9.23).

Supporting Information

Supporting Information is available from the Wiley Online Library or from the author.

Acknowledgements

Z.C., C.L., and X.Z. contributed equally to this work. K.P.L. thanks National Research Foundation, Singapore for NRF Investigator Award: "Graphene oxide a new class of catalytic, ionic and molecular sieving materials, award number: NRF-NRF12015-01." This work was supported by the National Natural Science Foundation of China (Project 51772110). All the authors thank the Analytical and Testing Center of Huazhong University of Science and Technology, the Wuhan National Laboratory for Optoelectronics. Z.C. and X.Z. thank the NGS Scholarship for support. The authors appreciate Lim Poh Chong and Dr. Tang Wei at A*STAR, IMRE for the GIXRD measurements and Liu Qiping at NUS for the HPLC tests.

Conflict of Interest

The authors declare no conflict of interest.

Keywords

confined catalysis, electrocatalysis, glycerol oxidation, graphene, platinum nanosheets

Received: July 25, 2018
Revised: October 8, 2018
Published online:

- [1] A. Corma, *Chem. Rev.* **1995**, 95, 559.
[2] S. M. Csicsery, *Zeolites* **1984**, 4, 202.
[3] N. Y. Chen, W. E. Garwood, *Catal. Rev.* **1986**, 28, 185.
[4] A. Corma, *J. Catal.* **2003**, 216, 298.
[5] J. Liu, L. Chen, H. Cui, J. Zhang, L. Zhang, C.-Y. Su, *Chem. Soc. Rev.* **2014**, 43, 6011.
[6] S. A. Miners, G. A. Rance, A. N. Khlobystov, *Chem. Soc. Rev.* **2016**, 45, 4727.
[7] D. Deng, K. S. Novoselov, Q. Fu, N. Zheng, Z. Tian, X. Bao, *Nat. Nanotechnol.* **2016**, 11, 218.
[8] Z. Y. Al Balushi, K. Wang, R. K. Ghosh, R. A. Vilá, S. M. Eichfeld, J. D. Caldwell, X. Qin, Y.-C. Lin, P. A. Desario, G. Stone, S. Subramanian, D. F. Paul, R. M. Wallace, S. Datta, J. M. Redwing, J. A. Robinson, *Nat. Mater.* **2016**, 15, 1166.
[9] J. Deng, D. Deng, X. Bao, *Adv. Mater.* **2017**, 29, 1606967.
[10] Q. Fu, X. Bao, *Chem. Soc. Rev.* **2017**, 46, 1842.
[11] D. Deng, X. Chen, L. Yu, X. Wu, Q. Liu, Y. Liu, H. Yang, H. Tian, Y. Hu, P. Du, R. Si, J. Wang, X. Cui, H. Li, J. Xiao, T. Xu, J. Deng, F. Yang, P. N. Duchesne, P. Zhang, J. Zhou, L. Sun, J. Li, X. Pan, X. Bao, *Sci. Adv.* **2015**, 1, e1500462.
[12] Z. Chen, K. Leng, X. Zhao, S. Malkhandi, W. Tang, B. Tian, L. Dong, L. Zheng, M. Lin, B. S. Yeo, K. P. Loh, *Nat. Commun.* **2017**, 8, 14548.
[13] Y. Luo, X. Li, X. Cai, X. Zou, F. Kang, H.-M. Cheng, B. Liu, *ACS Nano* **2018**, 12, 4565.
[14] Y. Yao, Q. Fu, Y. Y. Zhang, X. Weng, H. Li, M. Chen, L. Jin, A. Dong, R. Mu, P. Jiang, L. Liu, H. Bluhm, Z. Liu, S. B. Zhang, X. Bao, *Proc. Natl. Acad. Sci. USA* **2014**, 111, 17023.
[15] A. Messaoudi, R. Erre, F. Beguin, *Carbon* **1991**, 29, 515.
[16] A. V. Dunaev, A. I. Chikin, K. V. Pokholok, D. S. Filimonov, I. V. Arkhangel'skii, *Inorg. Mater.* **2010**, 46, 1084.
[17] J.-Y. Tilquin, R. Côté, G. Veilleux, D. Guay, J. P. Dodelet, G. Denès, *Carbon* **1995**, 33, 1265.
[18] K. J. Koski, C. D. Wessells, B. W. Reed, J. J. Cha, D. Kong, Y. Cui, *J. Am. Chem. Soc.* **2012**, 134, 13773.
[19] L. Bu, N. Zhang, S. Guo, X. Zhang, J. Li, J. Yao, T. Wu, G. Lu, J.-Y. Ma, D. Su, X. Huang, *Science* **2016**, 354, 1410.
[20] L. G. Verga, J. Aarons, M. Sarwar, D. Thompsett, A. E. Russell, C.-K. Skylaris, *Phys. Chem. Chem. Phys.* **2016**, 18, 32713.
[21] A. C. Ferrari, D. M. Basko, *Nat. Nanotechnol.* **2013**, 8, 235.
[22] J. Walter, J. Heiermann, G. Dyker, S. Hara, H. Shioyama, *J. Catal.* **2000**, 189, 449.
[23] W. Song, Z. Chen, C. Yang, Z. Yang, J. Tai, Y. Nan, H. Lu, *J. Mater. Chem. A* **2015**, 3, 1049.
[24] S. Chen, Z. Wei, X. Q. Qi, L. Dong, Y.-G. Guo, L. Wan, Z. Shao, L. Li, *J. Am. Chem. Soc.* **2012**, 134, 13252.
[25] Z.-Z. Jiang, Z.-B. Wang, Y.-Y. Chu, D.-M. Gu, G.-P. Yin, *Energy Environ. Sci.* **2011**, 4, 2558.
[26] R. P. Grandhiraman, D. Nordlund, C. Javier, J. E. Koehne, B. Chen, M. Meyyappan, *J. Phys. Chem. C* **2014**, 118, 18706.
[27] A. V. Dunaev, I. V. Arkhangel'skii, Ya. V. Zubavichus, V. V. Adveev, *Carbon* **2008**, 46, 788.
[28] K. Lochte, M. Fröba, F. Schulz, W. Me, *Mol. Cryst. Liq. Cryst. Sci. Technol., Sect. A* **1994**, 244, 245.
[29] Y. Holade, K. Servat, S. Tingry, T. W. Napporn, H. Remita, D. Cornu, K. B. Kokoh, *ChemPhysChem* **2017**, 18, 2573.
[30] H. Wang, L. Thia, N. Li, X. Ge, Z. Liu, X. Wang, *ACS Catal.* **2015**, 5, 3174.
[31] W. Hong, C. Shang, J. Wang, E. Wang, *Energy Environ. Sci.* **2015**, 8, 2910.
[32] S. Li, J. Lai, R. Luque, G. Xu, *Energy Environ. Sci.* **2016**, 9, 3097.
[33] Z. Bai, M. Shi, Y. Zhang, Q. Zhang, L. Yang, Z. Yang, J. Zhang, *Green Chem.* **2016**, 18, 386.
[34] A. Zalineeva, A. Serov, M. Padilla, U. Martinez, K. Artyushkova, S. Baranton, C. Coutanceau, P. B. Atanassov, *J. Am. Chem. Soc.* **2014**, 136, 3937.
[35] A. C. Garcia, M. J. Kolb, C. van Nierop, Y. Sanchez, J. Vos, Y. Y. Birdja, Y. Kwon, G. Tremiliosi-Filho, M. T. M. Koper, *ACS Catal.* **2016**, 6, 4491.
[36] D. J. Chadderton, L. Xin, J. Qi, B. Brady, J. A. Miller, K. Sun, M. J. Janik, W. Li, *ACS Catal.* **2015**, 5, 6926.
[37] L. Huang, J.-Y. Sun, S.-H. Cao, M. Zhan, Z.-R. Ni, H.-J. Sun, Z. Chen, Z.-Y. Zhou, E. G. Sorte, Y. Y. J. Tong, S.-G. Sun, *ACS Catal.* **2016**, 6, 7686.
[38] X. Huang, S. Tang, X. Mu, Y. Dai, G. Chen, Z. Zhou, F. Ruan, Z. Yang, N. Zheng, *Nat. Nanotechnol.* **2011**, 6, 28.
[39] H. Li, G. Chen, H. Yang, X. Wang, J. Liang, P. Liu, M. Chen, N. Zheng, *Angew. Chem.* **2013**, 125, 8526.
[40] H. Duan, N. Yan, R. Yu, C.-R. Chang, G. Zhou, H.-S. Hu, H. Rong, Z. Niu, J. Mao, H. Asakura, T. Tanaka, P. J. Dyson, J. Li, Y. Li, *Nat. Commun.* **2014**, 5, 3093.
[41] F. Sallem, Z. Zhang, B. Xu, X. Xu, P. He, X. Wang, *J. Am. Chem. Soc.* **2013**, 135, 18304.
[42] F. Sallem, B. Xu, B. Ni, H. Liu, F. Nosheen, H. Li, X. Wang, *Adv. Mater.* **2015**, 27, 2013.
[43] H. Li, J. Xiao, Q. Fu, X. Bao, *Proc. Natl. Acad. Sci. USA* **2017**, 114, 5930.
[44] Y. Du, Y. Zhu, S. Xi, P. Yang, H. O. Moser, M. B. H. Breese, A. Borgna, *J. Synchrotron Radiat.* **2015**, 22, 839.